



Hydrogen thermo-photo production using Ru/TiO₂: Heat and light synergistic effects



Uriel Caudillo-Flores^a, Giovanni Agostini^b, Carlo Marini^b, Anna Kubacka^{a,*}, Marcos Fernández-García^{a,*}

^a Instituto de Catálisis y Petroleoquímica, CSIC.C/Marie Curie 2, 28049, Madrid, Spain

^b Alba Synchrotron Light Source, Cerdanyola del Vallès, 08290, Barcelona, Spain

ARTICLE INFO

Keywords:

Thermo-photo-catalysis
Titania
Ruthenium
H₂ production
Quantum efficiency
Synergy of energy sources

ABSTRACT

A series of ruthenium – anatase solids with noble metal loadings from 1 to 10 wt. % was tested in the gas phase thermo-photo production of hydrogen using methanol as a sacrificial agent. Samples were characterized using X-Ray diffraction, UV-vis, X-ray photoelectron and absorption spectroscopies as well as transmission electron microscopy. A pure, high surface area anatase was present in all catalysts. It supports a ruthenium co-catalyst displaying a core-shell structure having an hcp metallic core and a RuO₂-type shell structure. Activity, particularly under the combined use of light and heat, was analyzed by means of “excess” functions; the reaction rate and the quantum efficiency of the process were studied for thermo-photo vs. thermo/photo processes to provide conclusive evidence that the ruthenium-anatase materials display a strong synergistic use of both energy sources when utilized simultaneously. Optimum thermo-photo performance was achieved with a 5 wt. % Ru/TiO₂ catalyst. An in-situ infrared study of the behavior of the gas-solid interface under the isolate or simultaneous action of heat and light was carried out to interpret the activity and analyze reaction mechanism. The study points out the key role of the ruthenium-anatase interface in activating carbon-containing species leading to carbon monoxide species subsequently transformed through a water gas shift type reaction. Activity seems directly correlated with the promotion of this step by light and heat within the context of a mechanism where methanol is previously oxidized in titania sites and such species evolves at the mentioned interface to generate hydrogen and carbon oxide molecules.

1. Introduction

Thermo-photo-catalysis is an exciting new field of research which attempts to combine thermal and light energy sources to carry out chemical process of industrial interest. Thermal (or conventional) catalysis is a mature research field presenting success in facilitating numerous environmental and energy-related catalytic reactions. A permanent challenge related to any catalytic material is to decrease its catalytic operation temperature (and pressure) as well as increasing the stability of the material [1]. Photo catalysis uses light as the energy source of the chemical process and has been also utilized in numerous chemical processes. It however owns a limited applicability mainly as a result of the low reaction rates and quantum efficiency [2,3]. The combination of the two energy sources may find attractive application in order to mitigate the main problems already mentioned for thermal or photo alone processes [4–7].

In this research field a key question (among others) is how simple

and effective is to combine classical heating with photonic excitation. Such a combination has been shown to decrease significantly the T₅₀, T₁₀₀ isoconversion temperature(s) for, for example, CO oxidation using Pt-TiO₂ [8], dye degradation using a CeO_x/CeO₂ powder [9], 2-propanol oxidation using CeO_x-TiO₂ catalysts [10] and oxidation of aromatics (benzene, toluene, xilenes) using Ag/SrTiO₃ systems [11]. The literature results show that using a moderate light intensity (around or below one tenth of milliwatts per square centimeter) important advantages in terms of activity as well as longevity of the catalyst can be achieved. The physical origin of such activity enhancement is unclear. Several factors would contribute positively in the catalytic output of thermo-photo active systems. In the case of metal-promoted titania catalysts, the handling of light wavelengths out of UV as well as local (localized) electric field and heating by plasmonic or other physical phenomena are frequently invoked [12,13]. For oxide-oxide systems the interface role, connected with or in parallel to the handling of anionic vacancies, are described as key properties for improving activity

* Corresponding authors.

E-mail addresses: ak@icp.csic.es (A. Kubacka), mfg@icp.csic.es (M. Fernández-García).

[6,9,10]. In addition to the physico-chemical properties above described, other important effects would be related to surface chemical effects in turn connected with the different reactivity originated by the involvement of excited (directly by light or by interaction with “excited” defects, etc.) species in specific reaction steps or changes in surface coverage(s) in presence/absence of light [4,6,8]. All these factors make complex the understanding of the underlying phenomena controlling activity in thermo-photo catalytic processes and claim for in-deep studies of the phenomenon.

In this work we used a ruthenium-promoted anatase-based catalyst formulation for analyzing the thermo-photo generation of hydrogen from methanol. Ru/TiO₂ systems has been previously reported as active materials in thermal [14] and photo [15–18] catalytic production of hydrogen. However, their use in a thermo-photo process is, to our knowledge, tested for the first time here. In this context, a first challenge is the analysis of the thermo-photo process output in comparison with both the thermal reaction at the corresponding temperature as well as the photo-catalytic reaction at room temperature. In order to provide a meaningful result, we presented an analysis of the excess measured in the reaction rate and quantum efficiency observables when comparing the thermo-photo with the combination of thermal and photo (corresponding) observables. Such analysis will be used to estimate the improvement obtained from both thermal and photonic perspectives of the activity. Besides that, we carried out a complete characterization of the materials with the help of UV-vis, X-ray diffraction, photoelectron and absorption (near edge XANES and extended fine structure EXAFS) spectroscopies as well as microscopy techniques. These tools were utilized to analyze structural and electronic properties of the catalytic solids, with emphasis in obtaining information about the ruthenium component. The study also presents an in-situ diffuse reflectance Fourier transform infrared study of the gas-solid interface under reaction (photo, thermal and thermo-photo) conditions. The combination of information coming from these three pieces highlights the significant advantages of the thermo-photo process with respect to thermal or photo alone process and provides a quantitative estimation for this issue. The work proposes that the synergistic utilization of light and heat for producing hydrogen using ruthenium-titania materials is based in the specific metal core – oxide shell of the ruthenium co-catalyst working together with the ruthenium – anatase interface. The interface contact of the ruthenium oxide defective (partially reduced) layer with anatase provides the adequate centers to open a route to decompose efficiently carbon-containing species and produce hydrogen through a complex mechanism. The interplay of charge and temperature in driving active center behavior at the interface seems at the core of the synergistic effect observed between the two energy sources. The dual function of ruthenium as well as the key role of the co-catalyst – anatase interface in the reaction mechanism appears thus unique features of the system and rationalizes the high thermo-photo activity of the materials.

2. Experimental

2.1. Catalysts synthesis

Titania support preparation was carried out in a propylene vial containing a mixture of 46.5 wt.% of ethanol (Industrial grade), 8.3 wt.% of titanium butoxide (Aldrich, 97.00%) and 45.2 wt.% of deionized water [19]. The mixture was transferred and heated at 160 °C under microwave irradiation by using a microwave reactor (Anton Paar, model Synthos 3000). The temperature was maintained for 2 min. The suspension obtained from de microwave reactor was atomized through a 2 mm nozzle in a YAMATO spray dryer (model DL410), at 2 bar and 200 °C. After drying, the samples received a thermal treatment at 600 °C in air during 1 h. Different amounts of RuCl₃·H₂O (1, 3, 5 and 10 wt.%) were added to a previously sonicate titania/water suspension. Afterwards, an appropriate volume of 0.1 mol/L NaBH₄ solution (molar

ratio, Ru: NaBH₄ = 1:5) was added to the mixture which was kept stirring for 1 h under N₂ atmosphere. Subsequently, the solid material was recovered by centrifugation and washed with mili-Q water. Finally, the materials were dried in an oven at 100 °C during 12 h. The nomenclature used to identify the different materials produced was: 1Ru/TiO₂, 3Ru/TiO₂, 5Ru/TiO₂ and 10 Ru/TiO₂. The numbers indicate the weight percentage (as measured by chemical analysis) of the ruthenium component expressed as Ru.

2.2. Characterization

Elemental analysis was determined using inductively coupled plasma atomic absorption spectroscopy (ICP-OES) (PerkinElmer Optima 3300 DV). A Seifert D-500 diffractometer equipped with Ni-filtered Cu K α radiation was employed to record XRD pattern of the as-synthesized samples with a 0.02° step. The particle sizes were estimated using XRD using the Williamson–Hall formalism [20]. UV-vis diffuse-reflectance spectroscopy experiments were performed on a Shimadzu UV2100 apparatus using nylon as a reference and the results presented as Kubelka–Munk transform [21]. Band gap analysis for the titania (anatase) indirect gap semiconductor was done following standard procedures; e.g. plotting $(hva)^n$ ($n = \frac{1}{2}$ or 2 for indirect or direct semiconductor; $h\nu$ = excitation energy, a = absorption coefficient) vs. energy and obtaining the corresponding intersection of the linear fit with the baseline [22]. Transmission electron microscopy images were taken in a JEOL 2100 F TEM/STEM microscope. UV-vis transmission or diffuse-reflectance spectra were recorded with a Shimadzu UV2100 apparatus (using BaSO₄ or Teflon as a reference for diffuse experiments).

XPS data were recorded on 4 × 4 mm² pellets, 0.5 mm thick, prepared by slightly pressing the powdered materials which were outgassed in the prechamber of the instrument at room temperature up to a pressure $< 2 \times 10^{-8}$ Torr to remove chemisorbed water from their surfaces. The SPECS spectrometer main chamber, working at a pressure $< 10^{-9}$ Torr, was equipped with a PHOIBOS 150 multichannel hemispherical electron analyzer with a dual X-ray source working with Ag K α ($h\nu = 1486.2$ eV) at 120 W, 20 mA. Survey spectra in the energy range from 0 to 1350 eV were recorded using 0.4 eV steps while high-resolution spectra were recorded with 0.1 eV steps, 100 ms dwell time and 25 eV pass energy. Curve fitting was carried out using the CasaXPS software in which aromatic carbon C1 s peak (284.8 eV) was used as the reference for binding energy calibration.

Transmission EXAFS measurements at Ru K-edge (22117 eV) were performed in quick-EXAFS mode at the CLAES beamline [23] of the Spanish National Light Source, (ALBA Synchrotron, Barcelona, Spain), using a Si(311) double-crystal monochromator. The incoming and outgoing photon fluxes were measured by ionization chambers filled with appropriate mixtures of N₂ and Kr gases. The second focusing mirror of the beamline has been set to have a focal point of $\sim 400 \times 300$ μm². Phase and amplitude functions were calculated using FEFF8.2 [24] and experimental factors ($S_0^{(2)}$) derived from reference materials (RuO₂ and Ru foil). Fitting results were obtained by using the VIPER program [25] and error bars were estimated with k¹/k²/k³ weighted fittings.

Diffuse Reflectance Infrared Fourier Transform Spectra (DRIFTS) were taken in a Bruker Vertex 80 FTIR spectrometer using a MCT detector and running under OPUS/IR software. The set-up consists of a praying mantis DRIFTS accessory (Harrick Scientific) and a reaction cell (HVC, Harrick Scientific). The reaction mixture was prepared by injecting in a nitrogen carrier (10 mL min⁻¹) a 3:7 alcohol:water mixture (0.15 mL min⁻¹) with a syringe pump before entering the DRIFTS cell. This mirrored the conditions at the reactor (see below). The DRIFTS spectra were collected in the range of 4000–600 cm⁻¹ with a resolution of 4 cm⁻¹. In DRIFTS experiments in-situ light excitation was carried out using 365 nm radiation. A Hg-Xe 500 W lamp with a dichroic filter 280–400 nm coupled with a 365 nm (25 nm half-width) filter (LOT-

Oriel) were used to select the light excitation. Each sample, without any previous treatment (expect flowing nitrogen for 10 min), was subjected in a continuous mode (without modifying gas mixture) to an experiment which aims to test the: *i*) dark conditions, *ii*) following evolution under illumination conditions. Experiments are carried out at room temperature (RT), 120, 180 and 240 °C. Spectra are presented as the difference of the spectrum taken at time t and the initial one (t = 0).

2.3. Thermo-photo catalytic measurements

The thermo-photo activity of the samples for methanol reforming was tested using a gas-phase continuous flow annular thermo-photo-reactor (pyrex) schematically depicted in Fig. S1. The catalyst (ca. 0.4 mg cm⁻²) was deposited onto the inner tube as a thin layer from a suspension in ethanol. During thermo-catalytic and thermo-photo-catalytic tests, the film was heated using a cartridge heater. The temperature of the layer was controlled and monitored by a temperature controller (Toho TTM-005) and K-type thermocouple inserted into the reactor. Minimal (below 1 °C) axial temperature variation was reached with a cartridge heater (230 V; 500 W; “Resistencias RSI INCOLOID800”) having controlled/compensated homogeneous heating. The UV irradiation was generated by four fluorescent UV lamps (Philips TL 6 W/08-F6T5 BLB, 6 W) symmetrically positioned outside the reactor. The reacting mixture 30:70 CH₃OH:H₂O (0.15 mL min⁻¹) was injected with a syringe pump in an Argon carrier flow (10 mL min⁻¹). The methanol to water ratio has been shown to maximized hydrogen production in Ru-based anatase catalysts [16]. The catalytic properties were evaluated at 3 h from the start of the irradiation, where a pseudo-stationary situation is reached. The concentrations of the reactant were analyzed using an online mass spectra (Onmistart 300) and gas chromatograph (Agilent GC 6890) equipped with HP-PLOT-Q/HP-Innowax columns (0.5/0.32 mm I.D. × 30 m) and thermal conductivity and flame ionization detectors.

In this work we measured catalytic output with the help of two observables, the reaction rate and the quantum efficiency. The reaction rate measured the number of hydrogen production molecules per surface area and time unit but to analyze the thermo-photo production of hydrogen we defined an “excess rate” measured trough Eq. (1) [10].

$$r_e = \text{rate (Thermo-photo)} - (\text{rate (Photo)} + \text{rate (Thermo)}) \quad (1)$$

Such “excess” rate measured the potential synergy occurring between both energy sources in the thermo-photo catalytic process. Synergy is thus measured as the excess (i.e. positive value) over the additive effect of light and heat in the reaction rate.

The second is the Quantum Efficiency (QE) parameter for hydrogen production. QE is defined by Eq. (2) [26].

$$QE(\%) = 100 \times \frac{2 \times r \text{ (mol m}^{-2}\text{s}^{-1})}{e^{a,s} \text{ (Einstein m}^{-2}\text{s}^{-1})} \quad (2)$$

In this equation, r is the reaction rate and e^{a,s} the average local superficial rate of photon absorption. The factor two consider the requirement of two electrons per hydrogen molecule. Here, for the calculation of the quantum efficiency we will use two different reaction rates, the normal ones and the excess one. The use of the latter would allow to measure an “excess” quantum efficiency.

The rate of hydrogen production is measured using mass spectrometry as previously outlined and normalized using the BET surface area of the sample. The local superficial rate of photon absorption (e^{a,s}) is defined by Eq. (3). It follows from the equation corresponding to a pure photo-catalytic process [27] but eliminating the losses coming from charge emission with temperature. In this equation F_{As} is the fraction of light absorbed by the sample q_{sup}, the radiation flux at each position (x ≡ X_s, Y_s, Z_s) of the catalytic film, and T_e is the thermal emission loss terminus.

$$e^{a,s}(x) = (q_{sup}(x) - T_e) F_{As} \quad (3)$$

To obtain the radiation flow on the surface of the samples, we calculate first the impinging radiation flux from the lamps (q_n). Considering the coordinate system presented in Fig. S1 and the geometry of the reactor (annular multilamp), the q_n can be determined by Eq. (4) [27].

$$q_n(X_s, Y_s, Z_s) = \sum_{L=1}^{L=4} \sum_{\lambda} \int_{\varphi_{min,L}(x,y)}^{\varphi_{max,L}(x,y)} \int_{\Theta_{min}(x,y,\varphi)}^{\Theta_{max}(x,y,\varphi)} \frac{P_{\lambda,L}}{2\pi R_L Z_L} \sin^2 \Theta \left(\left(\frac{X_s - X_L}{R} \right) \cos \varphi + \left(\frac{Y_s}{R} \right) \sin \varphi \right) d\varphi d\Theta \quad (4)$$

Where X_s, Y_s, Z_s are the coordinates of the points located on the surface of the catalytic films, and X_L, Y_L, Z_L which are the coordinates of the points located on the surface of the lamp. R type variables correspond to radius of the cylinder supporting the sample (R) or of the lamp (R_L), see Fig. S1. Angle variables (Θ, φ) are defined as described in Fig. S1. The integration limits can be evaluated using the ray tracing method [27], and are presented in the supporting information section.

Finally, the q_{sup} x/y components (see Fig. S1; Eq. (5)) can be determined using q_n and a radiation balance, which considers the main optical (Transmittance, F_i, and Reflectance, R_i) events occurring in all components of the reactor placed between the emission source and catalyst, i.e. glass and reaction media, as well on the catalytic film.

$$q_{sup}^{x,y} = f(q_n, F_i, R_i); i = \text{catalyst, glass, reaction media} \quad (5)$$

A detailed description of the mathematical formulation to provide q_{sup} as a function of q_n (Eq. (5)) and the transmittance/reflectance optical measurements for each component of our reactor system can be found elsewhere [27,28].

The T_e term can be calculated using equation S9 described at the supporting information section. This term is negligible at the temperatures of this work as it only makes a maximum correction of 4–5 parts per million to the local superficial rate of photon absorption values. This is at least 3–4 orders of magnitude below the standard error of the e^{a,s} coefficient. Such a result is somehow expected as emission losses in titania-based materials are known to occur at higher temperatures than here used [29].

3. Results and discussion

Fig. 1 illustrates the catalytic behavior of the solids in photo, thermal and thermo-photo conditions. As well known, the titania reference does not show significant activity in this reaction and the promotion of Ru boosts photo and thermal activity by several orders of magnitude [14–17]. Focusing on thermo-photo catalytic behavior, we

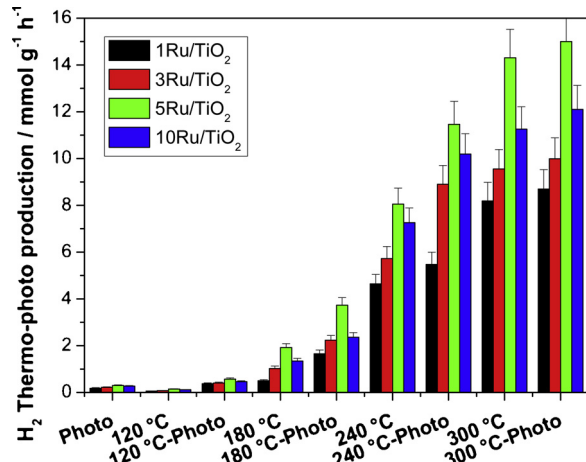


Fig. 1. Reaction rates values obtained in the Thermo-photo production of H₂ using a 3:7 CH₃OH:H₂O (v/v) ratio. Temperatures: RT, 120, 180, 240 and 300 °C.

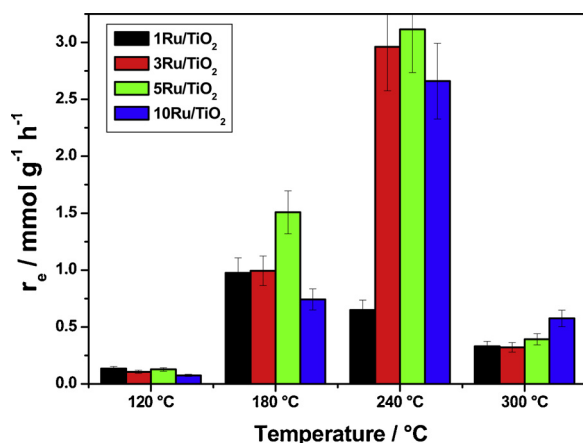


Fig. 2. Excess (reaction) rate obtained in the Thermo-photo production of H₂ using a 3:7 CH₃OH:H₂O (v/v) ratio.

Table 1

Values of the excess functions (rate and quantum efficiency) over the corresponding thermal and photo alone results. Experiments at 240 °C (except for the photo alone one).

Ratio	3Ru/TiO ₂	5Ru/TiO ₂
r_e/r	0.52	0.40
QE _{ex./QE}	13.8	10.6

can see an important response from the lowest temperature essayed. The corresponding rate is higher than the thermal counterpart in the whole range of temperatures analyzed, from 120 to 300 °C. For all operation conditions the 5Ru/TiO₂ seems to provide the higher reaction rates although in specific occasions other samples display close values. The thermo-photo catalytic behavior is further analyzed in detail in Fig. 2. Such figure contains data concerning the “excess” reaction rate defined by Eq. (1) (see also Fig. S2 for an extended temperature range). The excess rate demonstrates a clear synergistic effect between light and heat in our systems. Positive values of the excess rate are always obtained for all samples and they grow quickly with temperature up to 240 °C to decrease subsequently. Interestingly, the excess values indicate that 5Ru/TiO₂ sample displays always the higher synergistic effect and that, as mentioned, this reaches a maximum at 240 °C. At this temperature the 3Ru/TiO₂ sample shows a close value to the optimum. In fact, Table 1 shows that, considering the relative (and not the absolute as in Fig. 2) value of the thermo-photo response over the main thermo response, both samples (3 and 5Ru/TiO₂) display enhancement values (r_e/r) by ca. 40–50 %. This is a huge effect in thermal catalysis.

The thermal side analysis for the joint utilization of energy sources can be combined with the light one calculated with the help of the quantum efficiency observable. Quantum efficiency observables for the pure photo and thermo-photo reaction conditions are presented in Fig. 3. For the pure photo process, the optimum of Ru is ca. 30% superior to the optimum achieved with Pt (but of course, with lower amount of metal for the latter case) [16,30]. This indicates that, as suggested previously, Ru is a real alternative to Pt as co-catalyst in photonic processes concerning hydrogen production [15–17]. The quantum efficiency increases with temperature due to the minimal effect of the last physico-chemical variable in the superficial rate of photon absorption and the important effect in the reaction rate (Eq. (2)). Efficiency values thus grow with temperature and present a magnitude up to 2 orders of magnitude higher than the one of the photo alone process (Fig. 3). More importantly, Fig. 3 also includes data concerning the “excess” quantum efficiency calculated using Eq. (2) but utilizing the excess rate (Eq. (1)). Again, we observed that the 3 and 5Ru/TiO₂ samples display the maximum values for this observable,

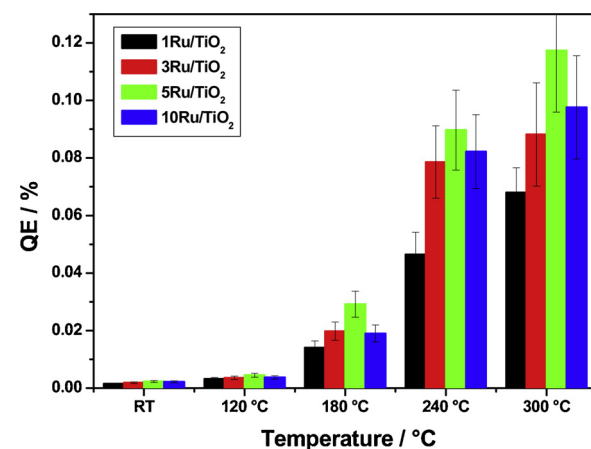


Fig. 2. Excess (reaction) rate obtained in the Thermo-photo production of H₂ using a 3:7 CH₃OH:H₂O (v/v) ratio.

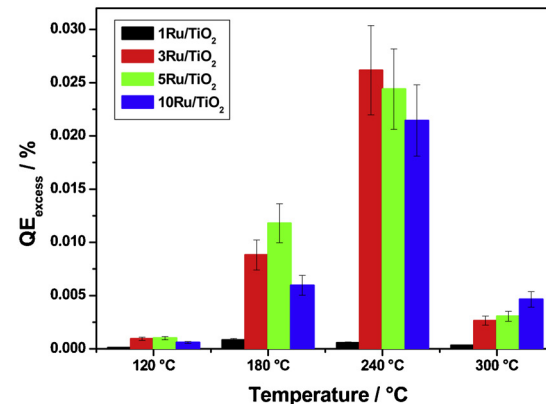


Fig. 3. Quantum efficiency and excess quantum efficiency values obtained in the Thermo-photo production of H₂ using a 3:7 CH₃OH:H₂O (v/v) ratio. Temperatures: RT, 120, 180, 240 and 300 °C. See text for details.

which grow up to 240 °C and then decreases. As measured by the excess observable, the excess efficiency presents a maximum at 240 °C. Note that the excess efficiency is higher than the photo alone observable. The relative value(s) included in Table 1 (the excess efficiency vs the efficiency of the photo alone process) show an optimum case for 3 and 5Ru/TiO₂ samples, with values exceeding ten. Comparison of the two observables of Table 1 indicates that from both a thermal and a photonic perspective the synergy of the two energy sources is rather important.

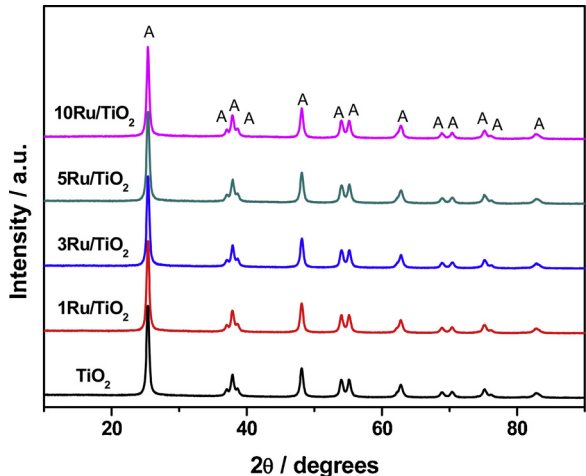
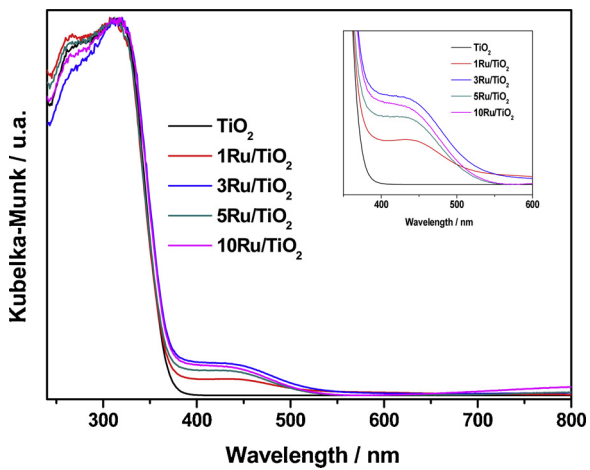
In order to study the selectivity of the methanol oxidation process and concomitant hydrogen production, the molar ratio between reaction products is summarized Table 2. Only carbon monoxide and dioxide are obtained as carbon-containing products for all samples and temperatures essayed under dark/illumination. The CO/CO₂ ratio increases with temperature and Ru loading and displays increasing sensitivity to illumination under reaction with the growth of the ruthenium content. CO₂ is the dominant product for all catalysts at low temperatures and CO production appears promoted by light except for the 1Ru/TiO₂ sample. The H₂/(CO + CO₂) ratio shows values between 0.2–0.4 under the exclusive action of light and a relative insensitivity to the Ru loading. The H₂/(CO + CO₂) ratio behavior parallels activity (Figs. 1 and 3) while increasing temperature in dark or under illumination, presenting larger values under the combined use of light and heat. The H₂/(CO + CO₂) ratio is maximized for the 5Ru/TiO₂ sample. Results of Table 2 are rationalized below with the help of the in-situ infrared analysis of the reaction.

To interpret the thermo-photo behavior we carried out a characterization study of the samples. XRD diffraction patterns of the active

Table 2

Molar ratios between reaction products of the reaction.

Temp. - Reaction	1Ru/TiO ₂		3Ru/TiO ₂		5Ru/TiO ₂		10Ru/TiO ₂	
	Molar Ratio ^a		CO/CO ₂		H ₂ /CO ₂		CO/CO ₂	
	CO/CO ₂	H ₂ /CO ₂	CO/CO ₂	H ₂ /CO ₂	CO/CO ₂	H ₂ /CO ₂	CO/CO ₂	H ₂ /CO ₂
Photo	0.0	0.2	0.0	0.3	0.0	0.4	0.0	0.4
120	0.1	0.1	0.1	0.1	0.1	0.2	0.1	0.1
120-Photo	0.1	0.4	0.2	0.5	0.3	0.6	0.3	0.5
180	0.2	0.5	0.5	0.9	0.7	1.4	1.0	0.8
180-Photo	0.2	1.1	0.6	1.4	0.9	2.1	1.5	1.0
240	0.7	1.6	1.8	1.1	2.4	1.9	2.8	1.5
240-Photo	0.6	1.9	2.0	1.7	3.2	1.9	4.4	1.6

^a Average standard error: CO/CO₂ ratio 8.7%; H₂/(CO + CO₂) 9.8%.Fig. 4. X-ray diffraction patterns of the Ru/TiO₂ samples.Fig. 5. UV-vis spectra of the Ru/TiO₂ samples.

TiO₂ support and Ru/TiO₂ photo-catalytic systems are displayed in Fig. 4. The analysis of the diffraction patterns only allowed the identification of Anatase phase; JCPDS card 78-2486, corresponding to the I41/amd space group. Absence of information considering the ruthenium component is noticed. The basic characterization of the samples was completed with the analysis of the main morphological properties of the samples (Table 3) and the UV-vis spectra (Fig. 5) of the solids. A relatively constant crystallite size of the anatase component (of ca.

Table 3Crystallite size, BET surface area, Pore volume, Pore size and Band gap values obtained from structural/porosity/optical measurements.^a

Sample	Crystallite size (nm)	BET surface area (m ² g ⁻¹)	Pore volume (cm ³ g ⁻¹)	Pore size (nm)	Band Gap (e ⁻ V)
TiO ₂	18.2	65.5	0.156	9.48	3.23
1Ru/TiO ₂	18.1	53.7	0.137	9.35	3.18
3Ru/TiO ₂	18.1	54.2	0.139	9.30	3.05
5Ru/TiO ₂	18.3	54.0	0.146	9.60	3.02
10Ru/TiO ₂	18.5	47.3	0.133	9.89	3.02

^a Average standard error: crystallite size 5.6%; BET area 4.8%; Band gap 3%.

18.1–18.5 nm) is observed together with a mild decrease of the BET surface area with the ruthenium content (Table 3). This could be justified by a partial occlusion of the anatase pores by the ruthenium component as evidenced by the pore size and volume behavior through the sample series. Considering the anatase component, the band gap values included in Table 3 display a modest decrease from the typical (bare) anatase value of 3.23 eV to ca. 3.02 eV for the 10Ru/TiO₂ material. Such a behavior was observed previously and ascribed to some electronic effect related to the strong interaction with ruthenium and anatase [15,16]. UV-vis spectra also informs about the ruthenium component. The broad hump observed in the near-UV-Visible region, after the typical decay related to the band gap of anatase, is characteristic of the Ru(IV) oxide. This oxide has plasmonic properties and would be identified by this spectroscopy [31,32]. To complete the characterization of the Ru component we combined microscopy, XPS and XAS tools.

Microscopy images are dominated by anatase nanoparticles of ca. 15–20 nm and well defined rounded shape. At the top of the anatase aggregated we can observe a significant number of ruthenium containing particles for all samples (see general views presented in panels A and D of Fig. 6). Fig. 6 shows general but also detailed micrograph views of selected solids. All micrographs confirm the fact that ruthenium entities are supported onto the anatase particles forming round shaped particles. The particle size distributions are presented in Fig. 7. This figure includes the mean particle diameter which goes from ca. 1.9 nm for the 1Ru/TiO₂ sample to ca. 5.7 nm for the 10Ru/TiO₂. The particle size distribution appears relatively narrow except in the 10Ru/TiO₂ solid. In spite of it, reasonable dispersion values are obtained for all materials, in consonance with similar studies [15,16]. The microscopy study is able to provide further details of the ruthenium component. In Fig. 8 we present detailed views of a few ruthenium containing nanoparticles of the 3Ru/TiO₂ and 5Ru/TiO₂ samples. In these cases we observed a differentiated core with higher atomic density and an outer shell with lower atomic density. Analysis of the diffraction planes indicates the presence of a ruthenium metallic core and a ruthenium oxide (RuO₂ type) shell. This is an experimental proof that the co-catalyst seems to have a dual chemical state, with a metallic nucleus protected by an oxidic shell.

The Ru/TiO₂ samples were also studied using XPS (Table S1). This corresponds to a relatively complex task taking into account that overlapping effects coming from close enough peak position(s) can be encountered between C-Ru (C 1s and Ru 3d) and Ru-Ti (Ti 2p and Ru 3p) contributions [16,33,34]. The latter is usually utilized due to lower overlapping problems and a summary of results is presented in Table S1. We detected the presence of Ti2p peaks at 458.1 and 458.8 eV, values typical of the Ti(IV) oxidation state [33,35]. The Ru component (ca. 280.6 eV; 3d_{5/2}) is ascribable to Ru(IV) in consonance with UV-vis results [16,33]. Although XPS pointed out a dominant presence of Ru(IV) at the surface of the ruthenium nanoparticles, the presence of metallic type phase can not be discarded due to above mentioned limitations of the XPS analysis and the relatively small difference of binding energy between Ru(0) and Ru(IV) [33]. Moreover, TEM

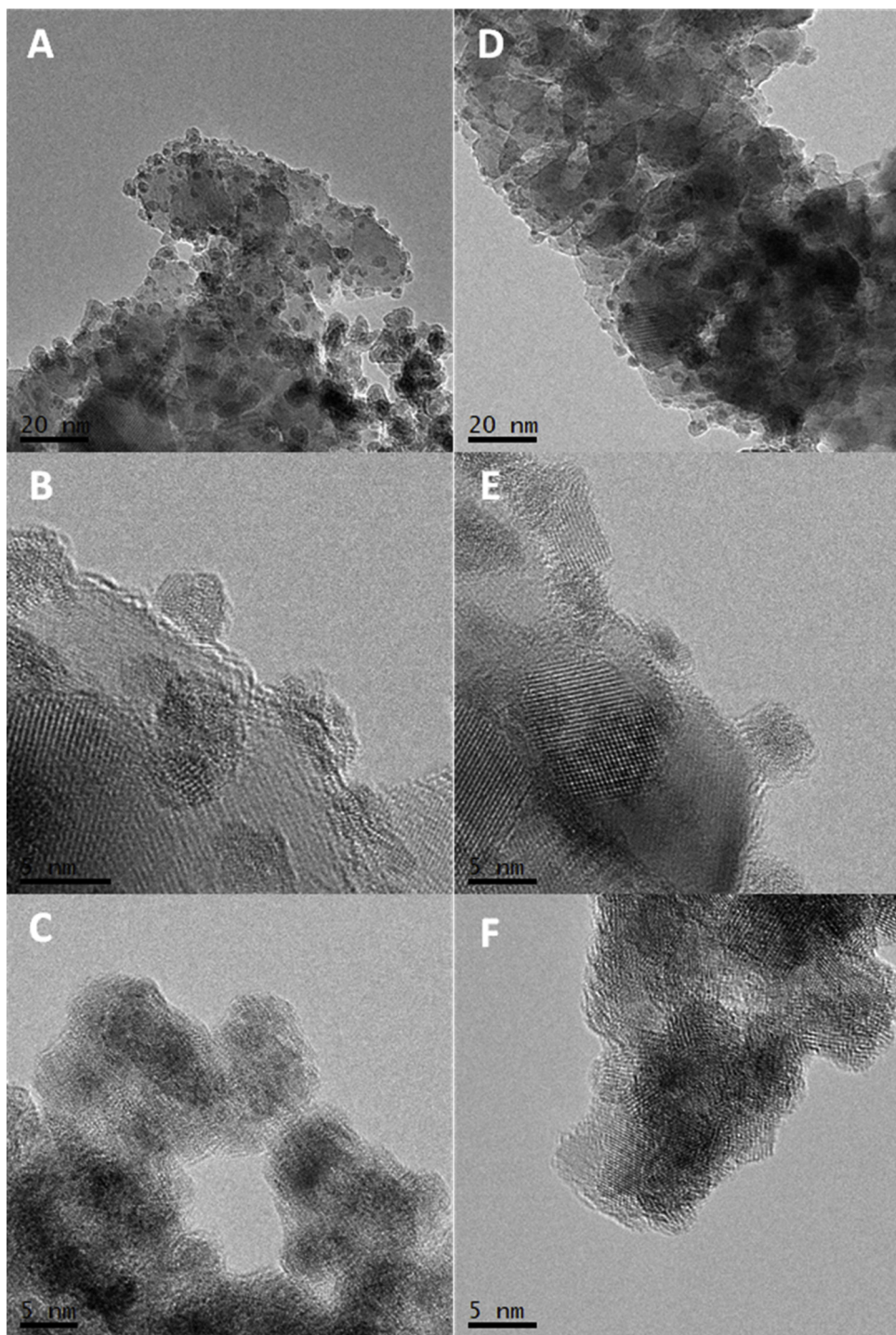


Fig. 6. TEM images of the 3Ru/TiO₂ (panels A–C) and 5Ru/TiO₂ (panels D–F) samples.

pointed out the presence of some type of core-shell ruthenium containing structures with simultaneous presence of an inner metallic and an outer oxidic phase(s). To unravel the situation we carried out a XAS study of the ruthenium component.

XANES and EXAFS signals for the Ru/TiO₂ samples are presented in Fig. 9. XANES spectroscopy informs about the average oxidation state of ruthenium in the samples [36,37]. Our samples own XANES spectra dominated by the oxide component but at the same time differing from it. The continuum resonance at ca 22160 eV broadens with ruthenium content while the one at ca. 22215 eV shift to lower energy. Both energy values are marked with dotted lines in Fig. 9 and their behavior

indicate, in consonance with previous techniques, the presence of a secondary (minor) metallic phase. We tested the amount of the different phases using a linear combination of the metallic and oxide references presented in Fig. 9. Fig. S3 illustrates however, the poor result obtained in this case. This is due to the size related effects, always present in XANES spectra [22,36,37]. Size effects strongly limit the usefulness of the linear combination method in this particular case. Nevertheless, using such methodology metallic ruthenium was (crudely) estimated to be ca. 16 mol. (Ru basis) % for 1Ru/TiO₂ to ca. 28% for 10Ru/TiO₂. A more reliable estimation is presented below using EXAFS.

A fitting procedure (briefly described in the experimental section)

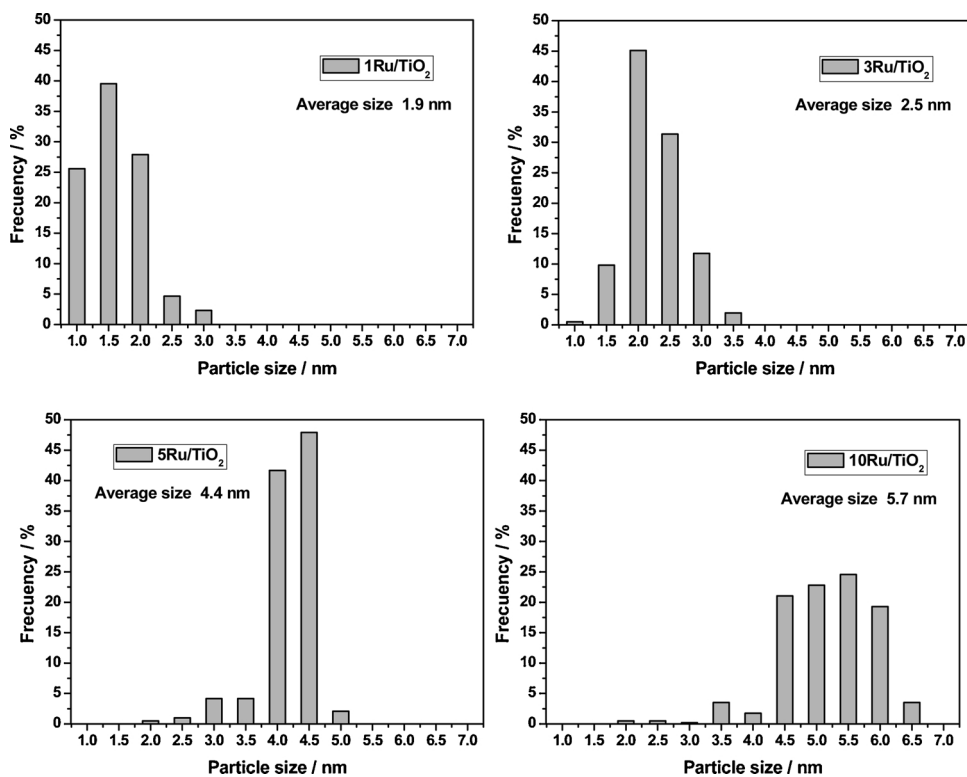


Fig. 7. TEM-derived particle size distribution of the ruthenium nanoparticles in the Ru/TiO₂ samples.

was applied to the EXAFS signals displayed in Fig. 9. Results from that fit are presented in Fig. 10 together with the (module and imaginary part of) k^2 -weighted fourier transform of the EXAFS signals. Fitting results are summarized in Table 4 which also includes (for each sample) the k and R fitting ranges as well as the free parameters allowed according to the Nyquist theorem [38]. The corresponding analysis indicates that the quality of the data allow the use of multiple shells (each defined by four parameters) for all samples. The 1Ru/TiO₂ is fully fitted using two coordination shells. The first is a Ru-O located at a distance of ca. 2.01 Å, characteristic of the RuO₂ rutile-type (P_{43}/mmm) phase [39]. The coordination number is however below the bulk [6] indicative of the epitaxial (or similar) deposition over a (metallic, see below) core. The low coordination number is thus another indication of the core-shell morphology of the ruthenium containing entities. The second shell at ca. 2.65 Å is characteristic of the hcp metallic ruthenium structure [40] and has a rather low coordination number of 1.8. For the

rest of samples we observe the presence of an additional, third shell. To confirm the meaningfulness of such shell in Fig. S4 we presented an F-test of the fitting differences encountered using 2 and 3 shell models of the samples. The statistical analysis reported at the supporting information section provides full evidence that all samples (except 1Ru/TiO₂) require the use of a 3 shell model to adequately simulate the EXAFS signal. Results of such 3-shell fittings are presented in Fig. 10 and numerically summarized in Table 4. The third shell detected corresponds in all cases to a Ru-Ru (called Ru-Ru ox. in Table 3) distance characteristic of the RuO₂ phase [39]. The coordination numbers of the Ru-O and Ru-Ru ox. shells indicates that the outer shell thickness grows with the ruthenium content of the materials. A similar conclusion (but now applied to the metallic counterpart) is achieved if considered the metal Ru-Ru coordination numbers. This is in agreement with the microscopy derived particle size distribution and can be used to estimate

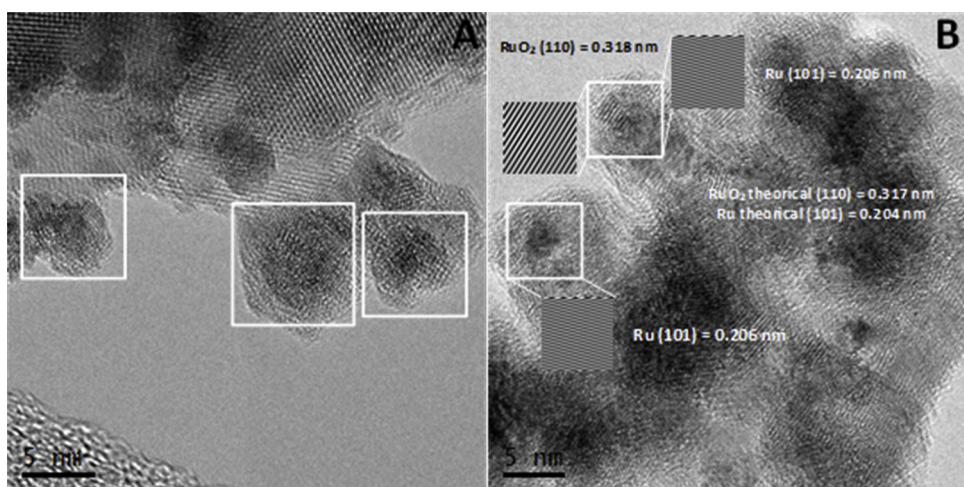


Fig. 8. Details of the ruthenium-containing core-shell structures presented in Ru/TiO₂ samples: 3Ru/TiO₂ (A) and 5Ru/TiO₂ (B).

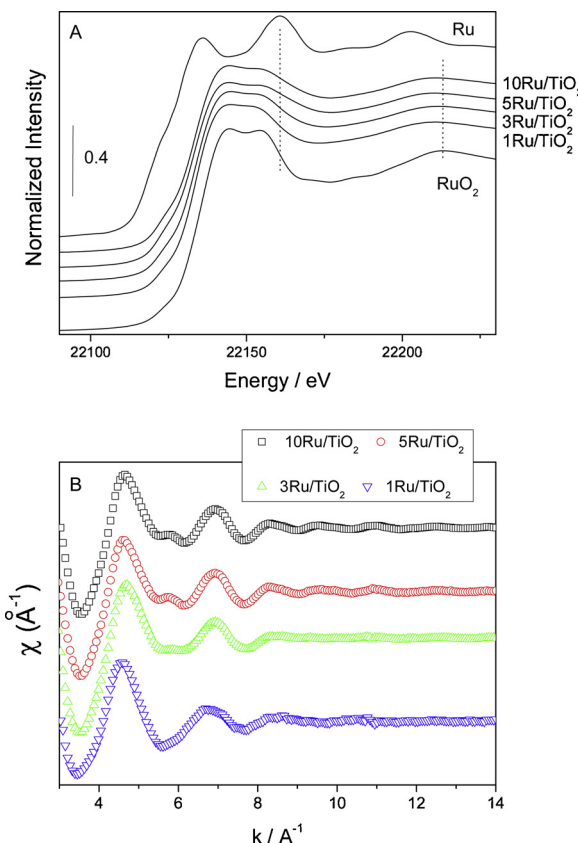


Fig. 9. Ru K-edge XANES (A) and EXAFS (B) spectra of the samples and reference systems. Spectra are shifted along the OY coordinate to help visualization.

the fraction of the metal (or oxide) components of ruthenium. Using this information we can establish that the fraction of metallic

ruthenium goes from ca. 20% for 1Ru/TiO₂ to ca. 34–38 % in 5 and 10Ru/TiO₂ samples. These values are higher than the ones obtained from XANES but are in semiquantitative agreement. So, the summary of the spectroscopic evidence, obtained by the combined use of UV-vis, XPS, XANES and EXAFS, allows to conclude that Ru has a core-shell structure with an outer surface, relatively defective, RuO₂-type layer and an internal hcp metallic core. Core-shell structures have been shown to become exceptional co-catalyst(s) in hydrogen production or water splitting due to the adsorption properties of the outer layer and the easy capture of electrons in turn connected with the existence of the metallic core [41–43].

To complete the study we carried out an in-situ study of the gas-solid interface using DRIFTS. In Fig. 11 DRIFTS spectra at dark conditions and under illumination are presented for the bare anatase support at room and higher temperatures. At room temperature and dark conditions we observed the adsorption of methanol with the development of a multipeak structure in the C–H stretching region (3000–2800 cm⁻¹) and the C–O stretch region (ca. 1170–1125 cm⁻¹). In fact, the double peak in the last region clearly indicates the presence of both physisorbed methanol and chemisorbed methoxy species [44,45]. We also observed a negative, broad band at ca. 1640 cm⁻¹ corresponding to desorption or displacement of water from the anatase surface and a sharp band at ca. 1380 cm⁻¹ could be assigned to the C–H asymmetric bending mode of the methanol [46]. Under illumination all methanol related vibrational modes show higher intensity but changes from dark spectra are relatively secondary. When the temperature rises, the C–H contributions show modest frequency shifts mainly originated from changes in organic coverage (by desorption or consumption and parallel elimination of water from the surface). Additional bands are observed. At dark conditions we detected additional, well defined bands at ca 1560 and 1440 cm⁻¹ and minor peaks at ca. 1380 cm⁻¹. The 1560 and ca. 1380 cm⁻¹ likely correspond to asymmetric and symmetric OCO stretching modes of bridge carboxylate (formate) species. The ca. 1440 cm⁻¹ is more difficult to identify unambiguously but can be ascribed to a CH₂ waving of bridging carboxylates or to other modes of (other) carboxylate/carbonate species [45–47]. In any case, when the temperature increases, the oxidation of methanol by water related

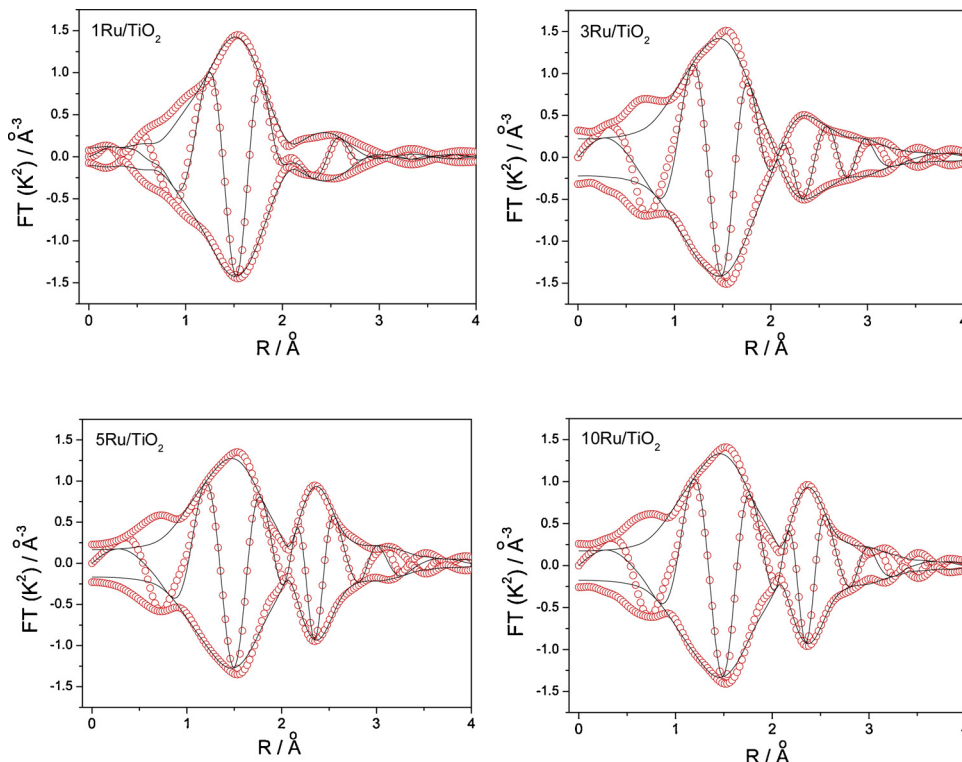


Fig. 10. Modulus and imaginary part of the k^2 -weighted Fourier Transform of the Ru K-edge EXAFS signal and fitting result for the samples. Red color circles: experimental curve; black color lines: fitting curves. (For interpretation of the references to colour in this figure legend, the reader is referred to the web version of this article).

Table 4

Fitting results of the Ru K-edge EXAFS signals. For each sample the k and R fitting ranges and number of free parameters are included.

Shell	Distance (Å)	C.N.	$10^3 \sigma^2 (\text{\AA}^2)$	E0 (eV)
1Ru/TiO ₂ k = 3.03-11.70 Å ⁻¹ ; R = 0.96-2.96 Å; 11				
Ru-O	2.01 ± 0.02	4.9 ± 0.5	6.1 ± 0.6	0.8 ± 0.6
Ru-Ru(m.)	2.65 ± 0.02	1.8 ± 0.1	7.6 ± 0.4	-3.9 ± 0.7
3Ru/TiO ₂ k = 3.03-13.58 Å ⁻¹ ; R = 0.96-2.96 Å; 13				
Ru-O	1.98 ± 0.02	6.1 ± 0.6	7.9 ± 0.6	2.5 ± 0.6
Ru-Ru(m.)	2.61 ± 0.02	2.8 ± 0.2	7.8 ± 0.7	-5.8 ± 0.9
Ru-Ru(ox.)	3.07 ± 0.02	2.7 ± 0.3	9.1 ± 1.1	2.1 ± 1.0
5Ru/TiO ₂ k = 3.03-14.41 Å ⁻¹ ; R = 0.96-2.96 Å; 14				
Ru-O	1.97 ± 0.02	5.8 ± 0.6	8.1 ± 0.6	0.5 ± 0.6
Ru-Ru(m.)	2.62 ± 0.01	3.5 ± 0.3	6.9 ± 0.5	-6.8 ± 0.9
Ru-Ru(ox.)	3.12 ± 0.02	3.3 ± 0.4	9.9 ± 1.4	0.6 ± 1.0
10Ru/TiO ₂ k = 3.03-14.45 Å ⁻¹ ; R = 0.96-2.96 Å; 14				
Ru-O	1.97 ± 0.02	5.9 ± 0.6	8.2 ± 0.6	0.1 ± 0.5
Ru-Ru(m.)	2.62 ± 0.01	3.7 ± 0.3	6.9 ± 0.5	-6.3 ± 0.9
Ru-Ru(ox.)	3.10 ± 0.02	3.9 ± 0.5	9.0 ± 1.3	0.3 ± 1.0

entities and concomitant presence of carboxylate type surface species becomes more obvious for both dark and illuminated conditions. No important differences are encountered at the different temperatures above room temperature presented in Fig. 11 and, essentially, illumination minimally differs from dark conditions, presenting nevertheless lower intensity for oxidized carbon-containing surface species.

When ruthenium is at the surface of anatase the behavior of the solid changes dramatically. To illustrate it we presented in Fig. 12 results for the 5Ru/TiO₂ solid (most active sample) and in Fig. 13 for the

$10\text{Ru}/\text{TiO}_2$ catalyst. All catalysts present (generally speaking) similar result and thus the comparison between these two catalysts is illustrative of the differences between samples. We first note that carboxylate and carbonate species only display weakly contributions for Ru/TiO_2 samples. Peaks are those previously presented for bare anatase and do not show differences between samples (and are thus omitted from the corresponding figures). More interesting results are observed together with the C-H stretching mode region as well as in the $2200\text{--}1700\text{ cm}^{-1}$ region. As the main difference with bare anatase, in the first region we observed the presence of a gas phase contribution centered at ca. $2840\text{ (a sharp peak) cm}^{-1}$. This is only accompanied with a broad bump at ca. 3680 cm^{-1} (water gas phase, results not shown) and 2140 cm^{-1} (CO gas, see below). Gas phase contributions (excluding water) are detected at $120\text{ }^\circ\text{C}$ for $5\text{Ru}/\text{TiO}_2$ and above $180\text{ }^\circ\text{C}$ for $10\text{Ru}/\text{TiO}_2$ (Figs. 12 and 13). Due to the reaction mechanism in which methanol is oxidized through a series of consecutive reactions [17,45–47], the most likely assignment of the 2840 cm^{-1} gas phase contribution is an aldehyde. The absence of other gas phase bands ascribable to organic molecules do not allow however a definitive assignment.

The second infrared region ($2200\text{--}1700\text{ cm}^{-1}$) mostly shows evidence of the formation of carbon monoxide species. At dark conditions and particularly at or above $120\text{ }^{\circ}\text{C}$ we detected the consumption of initially formed of bridged carbonyl species (ca. $1860\text{--}1850\text{ cm}^{-1}$) over metallic ruthenium surfaces [48]. Parallel formation of other carbonyls at $1950\text{--}1990$ and $2050\text{--}2060\text{ cm}^{-1}$, ascribable, respectively, to bridge and atop species, is detected for all samples [48,49]. Such contributions indicate the progressive reduction of the surface which, likely, is favored by the presence of the metallic core. Some frequency shifts for

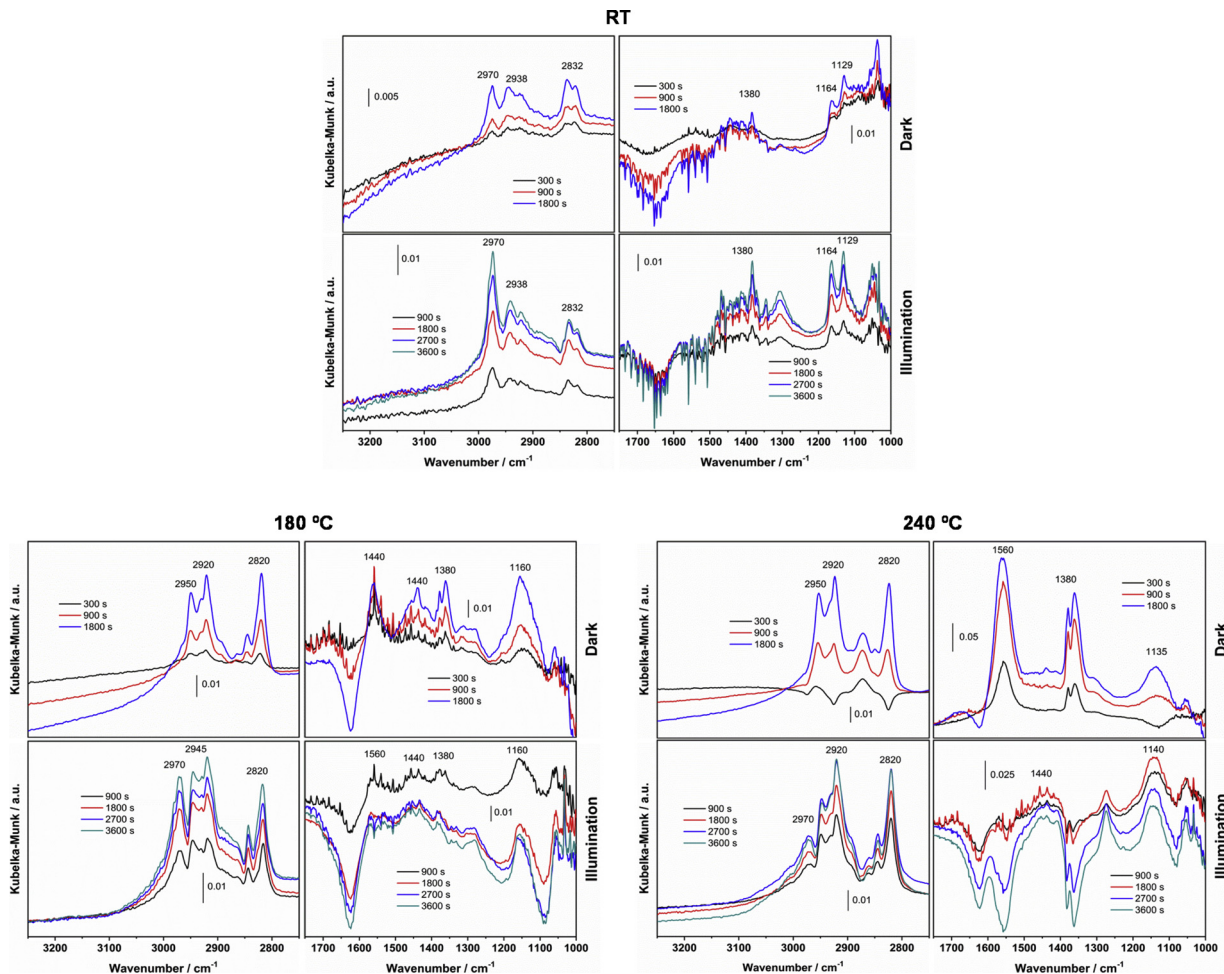


Fig. 11. DRIFTS spectra under dark and illuminated conditions obtained at different times for the TiO₂ sample.

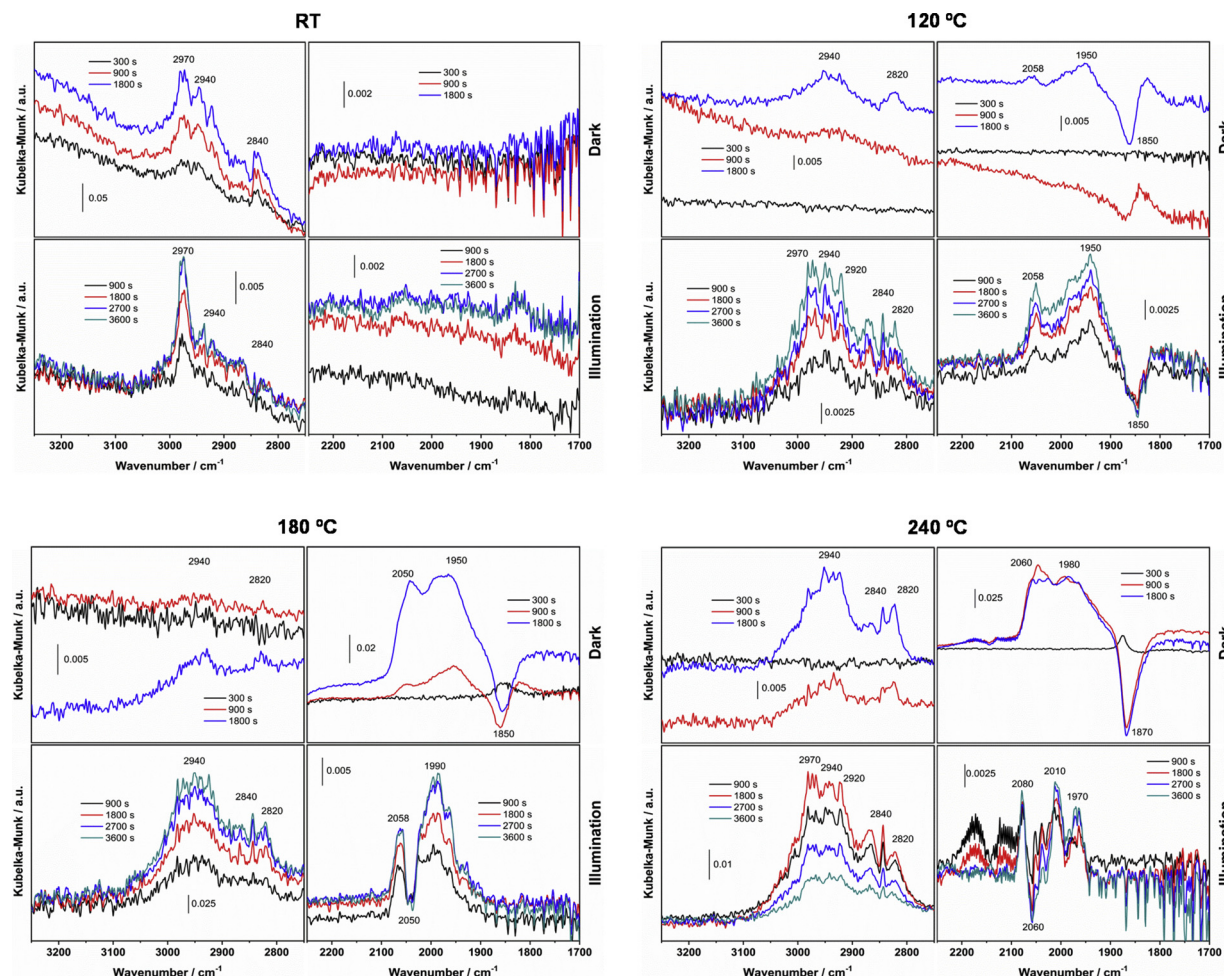


Fig. 12. DRIFTS spectra under dark and illuminated conditions obtained at different times for the 5Ru/TiO₂ sample.

carbonyl related species (within the limits already described) take place with temperature (and light) due to changes in coverage and concomitant dipolar coupling. Differences among samples up to 120 °C (but also at higher temperatures) correspond to the peak(s) intensity, as active is the sample as higher is the overall intensity of carbonyl species. At illuminated conditions we did not observe significant differences from dark conditions at 120 °C but some interesting changes occur at higher temperatures. At such temperatures the plots indicates that atop carbonyl species at ca. 2060-2050 (5Ru/TiO₂) and 2050-2020 (10Ru/TiO₂) cm⁻¹ are quickly consumed. Such species seems thus directly involved in the light promotion of the water gas shift type reaction, responsible for boosting the generation of hydrogen and carbon dioxide. As mentioned, main differences among samples are related to the intensity of the signals and the predominance of the high wavelength counterpart, 2060-2050 cm⁻¹, in the most active 5Ru/TiO₂ material. Note also that CO gas (2140 cm⁻¹) and adsorbed species over titania (ca. 2175-2120 cm⁻¹; see ref. 50) produced by spillover could be additionally observed in 5Ru/TiO₂ (Fig. 12), again indicating the most efficiency evolution of the surface (particularly carboxylate) species in the way to hydrogen.

So, the carbon-containing species activated in the anatase surface suffer a characteristic evolution to produce hydrogen in presence of ruthenium species. Samples display essentially the same reaction mechanism in respect to the infrared results with small variations related to differences of the surface of the ruthenium component surface microstructure which facilities partial reduction of the RuO₂-type surface and appearance of different surface sites according to CO (which can be used as a probe of the surface morphology). Optimum activity at dark

conditions is connected with the maximum production of carbon monoxide and thus with the evolution of the carbon-containing species (likely at the ruthenium – anatase interface) initially activated in the anatase support. Light seems to promote the activity at temperatures at or above 120 °C by effectively promoting the activity of specific ruthenium local entities involved in the evolution of carbon monoxide, through a water gas shift reaction. Such step may be carried out with hydroxyl related entities excited by light. The physico-chemical ground behind the ruthenium promoting role of the reaction under illumination is complex to analyze but the plasmonic (plus local temperature effects) properties of our core-shell nanoparticles may be significant. As a simple test to investigate it, we tested the reaction under visible illumination (above 420 nm) where near null activity is observed at room temperature (Table S3). At 180 °C and for the 5Ru/TiO₂ sample we observed an illumination/dark reaction rate enhancement for both UV and visible illumination, as detailed in Table S3. So the plasmonic (and concomitant local heating associated effects) properties of the partially oxidized ruthenium shell would thus contribute to the important synergistic effect observed in the activity under thermo-photo conditions [5,6]. The catalytic role of the ruthenium component also extends to the use of the metallic core as electron reservoir facilitating charge separation under illumination and the coupling of protons [6,18]. The metallic core of the ruthenium entities reaches a relatively stable dimension according to XAS results for the 5Ru/TiO₂ sample, a fact which would be also contributing to the optimization of the catalytic activity observed for this sample.

To strengthen the analysis of the mechanism and, particularly, to analyze the origin of the carbon monoxide and its evolution under

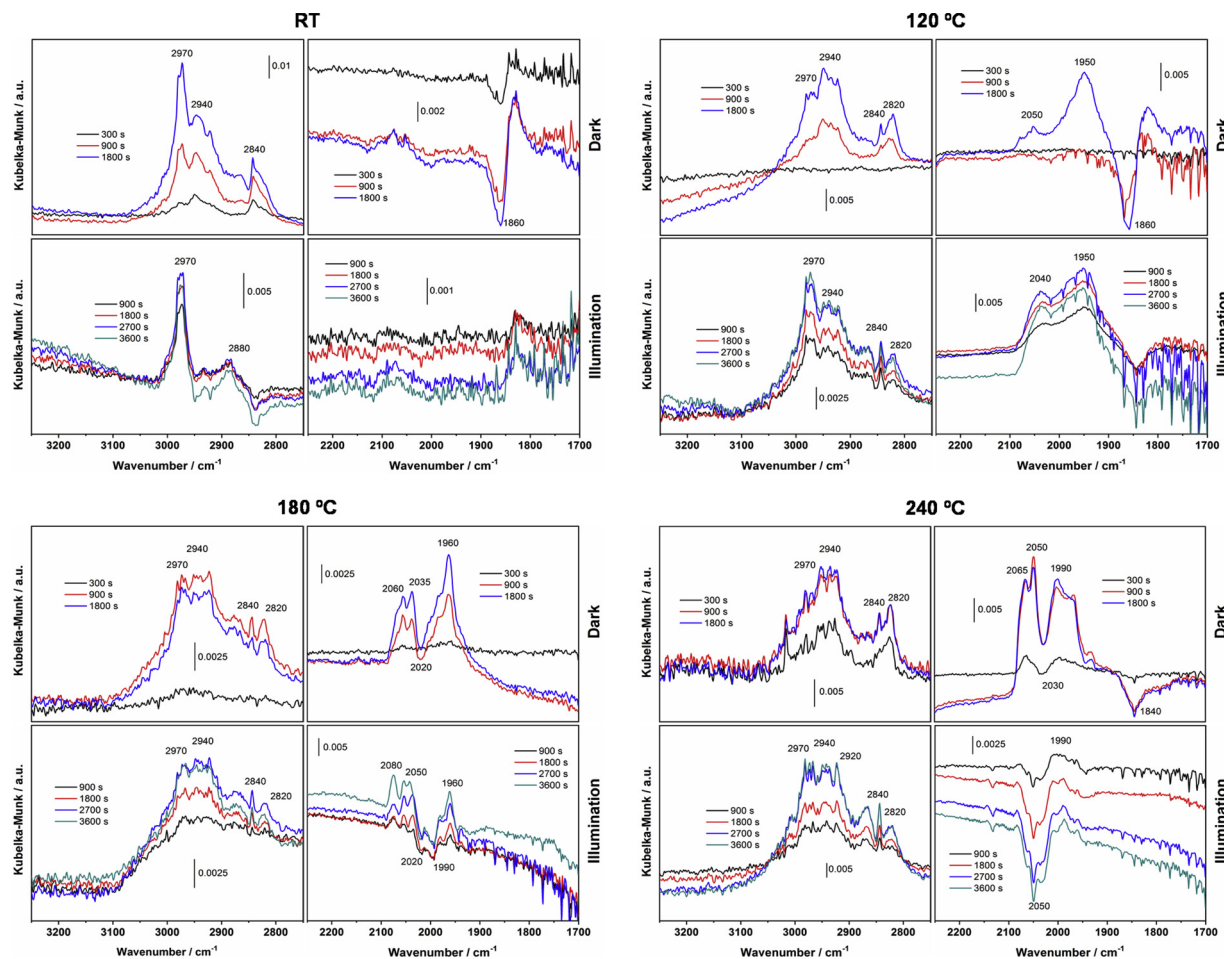
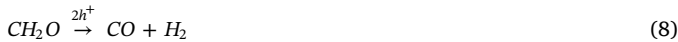


Fig. 13. DRIFTS spectra under dark and illuminated conditions obtained at different times for the 10Ru/TiO₂ sample.

reaction we carried out an infrared analysis of the main intermediates described in the literature. As mentioned, the hole-related species attack to the methanol molecule takes place with production of progressively oxidized species and formation of formaldehyde and formic acid (and corresponding surface adsorbed species). These steps are described in Eqs. (6) and (7). Protons (hydrogen) are concomitantly produced. These two steps/reactions occur at dark and can be promoted under illumination by the above mentioned hole related species [17,18,45–47,51,52].



We measured the infrared signal after contacting the catalyst(s) with formaldehyde and formic acid solutions in water (using organic concentration as dictated by the reaction rate previously measured for methanol and a 1:1 conversion according to Eqs. (6) and (7) –upper concentration limit possible for both species). Representative results are presented at dark and under illumination at 180 °C and using the most active sample (5Ru/TiO₂) in Fig. S5 for formaldehyde and Fig. S6 for formic acid.

In the case of formaldehyde, peaks at the C-H region (3200–

2700 cm⁻¹) indicate the aldehyde adsorption on the titania surface [53]. Interestingly, the carbonyl region (ca. 2250–1700 cm⁻¹) shows a strong similitude with spectra obtained at different contact times under the reaction mixture (Fig. 12). The initial formation of a bridged-bonded ruthenium carbonyl at 1850–1860 cm⁻¹ is followed by its disappearance (already at dark conditions) with production of additional bands corresponding bridged (1950–1990 cm⁻¹) and atop (2050–2060 cm⁻¹) carbonyl species [48,49]. In Fig. S5 and under illumination we observed the (additional) consumption of formaldehyde (C-H region) indicating that Eq. (6) is promoted by light. In addition in the carbonyl region we observed a rather similar behavior to Fig. 12, with consumption of specific carbonyl species peaking at ca. 2040–2060 cm⁻¹. The almost identical behavior displayed in the carbonyl region of Figs. S4 and 12 strongly indicates that formaldehyde would be the main precursor for the CO species detected under reaction conditions. Formaldehyde is considered to evolve in the surface of the catalysts through the production of formates and subsequent formation of carbon oxides [53].

To test the importance of formate species, which on the other hand are the main (aside methanol) carbon-containing species detected under reaction conditions (Figs. 10–12), we also analyzed the evolution of species coming from formic acid. At dark conditions, Fig. S6 analyzes this point showing first the relatively weak adsorption, characteristic of the acid, as demonstrated by the weak C-H contribution at ca. 2960 cm⁻¹ [54]. Interestingly, we only detected the bridged-bonded carbonyl species at ca. 1855 cm⁻¹ species [48]. Under illumination this last species displays a shift to higher wavenumbers (remember that IR spectra are differences) without any additional modification. This carbonyl species is the one initially observed for formaldehyde (and under

reaction conditions for the methanol:water mixture, Fig. 12) which suggests that Eq. (8) may not be the only one producing carbon monoxide and that an additional path would consider surface reactions which can be represented by Eq. (7), oxidation of formaldehyde to formic acid related species, and Eq. (9), the decomposition of such species producing carbon monoxide as previously observed in Pt-TiO₂ powders [45,47]. All [7–9] steps but, particularly, steps 7 and 8 seem promoted by light according to infrared results. Finally, in presence of a metal as ruthenium, the co-presence of CO (CO₂) and hydrogen occurs under the water gas shift equilibrium, equation 10 [55,56]. The final outcome is the production of hydrogen with carbon dioxides.

The analysis of the selectivity issues presented in Table 2 indicates that, as a general rule, increasing of the temperature of reaction triggers an increase of the CO/CO₂ ratio and H₂/(CO + CO₂) ratios, which could be ascribed to the increasing importance of CO production by Eq. (8) vs. (9). Combination of heat and light follows roughly the same behavior. Comparing thermal alone and thermo-photo results we can observe that at low temperatures (among those essayed) modest increases of the CO/CO₂ ratio trigger important increases of the H₂/(CO + CO₂) ratio, a fact ascribable to a combined effect of enhancing the pathway corresponding to Eq. (8) (vs. (9)) and the activation (increasing importance by using OH-related radical species together with or alternatively to water) of the water gas shift reaction, Eq. (10). The catalytic behavior becomes more complex around or above 180 °C where there is increasing quantities of CO and particularly different behavior as a function of Ru content. In this temperature region, the limitation in the relative (heat + light vs. heat) H₂/(CO + CO₂) ratio behavior would indicate that Eqs. (8) and (9) are both active.

4. Conclusions

A series of Ru/TiO₂ samples with increasing quantities of the co-catalyst were utilized in the thermo-photo production of hydrogen from methanol. The materials contain a pure high surface area anatase oxide as support. The multitechnique analysis of the solids demonstrates that the ruthenium component has nanoparticles from ca. 1.9 nm for the 1Ru/TiO₂ to ca. 5.7 nm for 10Ru/TiO₂. In all cases, such nanoparticles display core-shell morphology with a hcp metallic core and an outer RuO₂-type layer. XAS demonstrate that, at least for low loadings, the growth of the outer layer has some kind of epitaxy and defective character.

The activity of the Ru/TiO₂ samples show a strong synergistic effect when light and heat are used jointly as energy source of the hydrogen production process. Maximum thermo-photo effect is achieved for the 5Ru/TiO₂ at 240 °C with significant advantages from the use of thermal or photonic alone energy sources. The calculation of the excess reaction rate and efficiency demonstrates that the synergy occur from both sides the thermal and the photonic ones. To interpret the catalytic behavior we carried out an in-situ infrared study of the reaction under light, heat or the combination of both. The vibrational analysis demonstrates that carbon containing fragments as carboxylates, produced from methanol at the titania surface, suffer evolution at the ruthenium-anatase interface to generate carbon monoxide which further evolves to produce hydrogen through a water gas shift type reaction. Ru/TiO₂ solids operate with essentially the same general reaction mechanism in absence or under the (additional) influence of light. The general mechanism of the reaction analyzed with infrared spectroscopy, outlined in Eqs. (6)–(10), supports a step like oxidation of methanol with evolution of surface formaldehyde-type species through formate-type species and/or CO, followed by the water gas-shift reaction. All steps except 9 generate hydrogen and all seem promoted by light and/or heat to different extent. Differences between samples seem related to the microstructure of the surface ruthenium component, its reducibility and charge handling properties (this last in turn connected with both the metal core electron handling as well as plasmonic-related effects of the oxide shell), and the joint effect with the support in the generating and handling of carbon

monoxide and subsequent production of hydrogen.

Acknowledgments

Authors are thankful to “Ministerio de Ciencia, Innovación y Universidades” (Spain) for supporting the work carried out through the ENE2016-77798-C4-1-R grant. M. F.-G. thank Prof. F. Fernández-Martín for fruitful discussions. The support by Secretaría de Educación, Ciencia, Tecnología e Innovación of CDMX (SECTEI, México. U. Caudillo-Flores) is also acknowledged. Alba synchrotron is acknowledged for the beamtime.

Appendix A. Supplementary data

Supplementary material related to this article can be found, in the online version, at doi:<https://doi.org/10.1016/j.apcatb.2019.117790>.

References

- [1] H. Olivier-Boubigou, et al., ChemCatChem 9 (2017) 1–37.
- [2] A. Kubacka, M. Fernández-García, G. Colón, Chem. Rev. 112 (2012) 1555–1614.
- [3] J.C. Colmenares, R. Luque, Chem. Soc. Rev. 43 (2014) 765–778.
- [4] M.-Q. Yang, M. Gao, M. Hong, G.W. Ho, Adv. Mater. (2018) 1802894.
- [5] M. Ghoussoob, M. Xia, P.N. Duchesne, D. Segal, G. Ozin, Energ. Environ. Sci. 12 (2019) 1122–1142.
- [6] V. Nair, M. Muñoz-Batista, M. Fernández-García, R. Luque, J.C. Colmenares, ChemSusChem 12 (2019) 2098–2116, <https://doi.org/10.1002/cssc.201900175>.
- [7] M. Selva, R. Luque, Curr. Op. Green Sust. Chem. 15 (2019) 98–102.
- [8] Y. Zhou, D.E. Doronkin, Z. Zhao, Ph.N. Plessow, J. Jlić, B. Detlefs, T. Pruessmann, F. Stütz, J.-D. Grunwaldt, ACS Catal. 8 (2018) 11398–11406.
- [9] R. Verma, S.K. Samdarshi, S. Bojja, S. Paul, B. Choudhury, Sol. Energy Mater. Sol. Cells (2019) 141.
- [10] M.J. Muñoz-Batista, A.M. Eslava-Castillo, A. Kubacka, M. Fernández-García, Appl. Catal. B 225 (2018) 298–306.
- [11] W. Ji, T. Slem, J. Kong, Y. Tong, Ind. Eng. Chem. Res. 57 (2018) 12766–12773.
- [12] Y. Nishijima, K. Ueno, Y. Kotake, K. Murakoshi, H. Inoue, H. Misawa, J. Phys. Chem. Lett. 3 (2012) 1248–1252.
- [13] X. Zhang, X. Ke, J. Yao, J. Mater. Chem. A 6 (2018) 1941–1966.
- [14] P. Tahay, Y. Khani, M. Jabari, F. Bahadoran, N. Safari, Appl. Catal. A 554 (2018) 44–53.
- [15] G. Gu, J. Long, L. Fan, L. Chen, L. Zhao, H. Lin, X.J. Wang, Catal. 303 (2013) 141–155.
- [16] W. Ouyang, M. Muñoz-Batista, A. Kubacka, R. Luque, M. Fernández-García, Appl. Catal. B 238 (2018) 434–443.
- [17] H. Wang, Y. Liu, R. Li, Z. Yang, X. Zhang, H. Wang, Liu, Chem. Comm. 55 (2019) 2781–2784.
- [18] V. Kumaravel, S. Matthew, J. Barlett, S.C. Pillai, Appl. Catal. B 244 (2019) 1021–1064.
- [19] U. Caudillo-Flores, M.J. Muñoz-Batista, F. Ung-Medina, G. Alonso-Núñez, A. Kubacka, J.A. Cortés, M. Fernández-García, Chem. Eng. J. 299 (2016) 393–402.
- [20] G.K. Willianson, W.H. May, Acta Metall. 1 (1953) 22–29.
- [21] P. Kubelka, J. Op. Soc. Am. 38 (1948) 448–457.
- [22] M. Fernández-García, A. Martínez-Arias, J.C. Hanson, J.A. Rodriguez, Chem. Rev. 104 (2004) 4063–4105.
- [23] L. Simonelli, C. Marini, W. Olszewski, M. Ávila-Pérez, N. Ramanan, G. Guilera, V. Cuartero, K. Clementiev, Cogent Phys. 3 (2016) 1231987.
- [24] The FEFF Project - FEFF, (2019) (n.d.). Retrieved 9 February 2018, from, <http://monalisa.phys.washington.edu/feffproject-feff-xafsdataanalysis.html>.
- [25] K.V. Clementev, J. Phys. D Appl. Phys. 34 (2001) 209–214.
- [26] S.E. Braslavsky, A.M. Braun, A.E. Cassano, A.V. Emeline, M.I. Litter, L. Palmisano, V.N. Parmon, N. Serpone, Pure Appl. Chem. 83 (2011) 931–1014.
- [27] M.J. Muñoz-Batista, A. Kubacka, A.B. Hungría, M. Fernández-García, J. Catal. 330 (2015) 154–166.
- [28] G.E. Imoberdorf, H.A. Irazoqui, A.E. Cassano, O.M. Alfano, Ind. Eng. Chem. Res. 44 (2005) 6075–6085.
- [29] J. Xhen, P. Vincent, N.P. Blanchard, J. Nicolle, M. Choueib, V. Salles, A. Brioude, J. Vac. Sci. Technol. 30 (2012) 011801.
- [30] U. Caudillo-Flores, M.J. Muñoz-Batista, J.A. Cortés, A. Kubacka, M. Fernández-García, Molec. Catal. 437 (2017) 1–10.
- [31] M.A. Asi, C. He, M. Su, D. Xia, L. Lin, H. Deng, Y. Xiong, R. Qiu, X. Li, Catal. Today 175 (2011) 256–263.
- [32] M.T. Uddin, Y. Nicolas, C. Olivier, L. Servant, T. Toupane, S. Li, A. Klein, W. Jaegermann, Phys. Chem. Chem. Phys. 17 (2015) 5090–5102.
- [33] C.D. Wagner, Handbook of X-ray Photoelectron Spectroscopy: a Reference Book of Standard Data for Use in x-ray Photoelectron Spectroscopy, Physical Electronics Division, Perkin-Elmer Corp., 1979.
- [34] Q. Gu, Z. Gao, S. Yu, C. Xue, Adv. Mater. Interfaces 3 (2016) 17–21.
- [35] M.J. Muñoz-Batista, A. Kubacka, M.N. Gómez-Cerezo, D. Tudela, M. Fernández-García, Appl. Catal. B Environ. 140–141 (2013) 626–635.
- [36] M. Fernández-García, Catal. Rev. Sci. Eng. 44 (2002) 59–121.

- [37] T. Yamamoto, X-ray Spectrom. 37 (2008) 572–584.
- [38] Report on Fitting Procedures of the “Error Analysis Committee”, (2019) at http://ixs.csrr.iit.edu/IXS/subcommittee_reports/.
- [39] T. Arikawa, Y. Takasu, Y. Murakami, K. Asakura, Y. Iwasawa, J. Phys. Chem. B 102 (1998) 3736–3741.
- [40] A.M. Karim, V. Prasad, G. Mpourmpakis, W.W. Lonergan, A.I. Frenkel, J.G. Chen, D.G. Vlachos, J. Am. Chem. Soc. 131 (2009) 12230–12239.
- [41] X. Chen, S.S. Chen, L. Guo, S.S. Mao, Chem. Rev. 110 (2010) 6503–6570.
- [42] K. Maeda, K. Domen, J. Phys. Chem. Lett. 1 (2010) 2655–2661.
- [43] Y. Ma, X. Wang, Y. Jia, X. Chen, H. Han, C. Li, Chem. Rev. 114 (2014) 9987–10043.
- [44] P.A. Panatoyov, S.T. Burrows, J.P. Morris, J. Phys. Chem. C 116 (2012) 6623–6635.
- [45] O. Fontelles-Carceller, M.J. Muñoz-Batista, E. Rodríguez-Castellón, J.C. Conesa, M. Fernández-García, A. Kubacka, J. Catal. 347 (2017) 157–169.
- [46] M. El-Roz, P. Bazin, F. Thibault-Starzyk, Catal. Today 205 (2013) 111–119.
- [47] U. Caudillo-Flores, M.J. Muñoz-Batista, M. Fernández-García, A. Kubacka, A. Appl. Catal. B 238 (2018) 533–545.
- [48] S.Y. Chin, C.T. Willians, M.D. Amiridis, J. Phys. Chem. B 110 (2006) 871–882.
- [49] T. Yajima, H. Uchida, M. Watanabe, J. Phys. Chem. B 108 (2004) 2654–2659.
- [50] L. Mino, G. Spoto, S. Bordiga, A. Zecchina, J. Phys. Chem. C 117 (2013) 11186.
- [51] O. Fontelles-Carceller, M.J. Muñoz-Batista, J.C. Conesa, M. Fernández-García, A. Kubacka, Appl. Catal. B 216 (2017) 133–145.
- [52] L. Glarizia, D. Russo, I. Di Somma, R. Endreozzi, R. Marota, Energies 10 (2017) 1624–1648.
- [53] L. Wang, H. Yue, Z. Hua, H. Wang, X. Li, L. Li, Appl. Catal. B 219 (2017) 301–313.
- [54] M. Keulmans, S.W. Verbruggen, B. Haucheme, J.A. Martens, S. Lenaerts, J. Catal. 344 (2016) 221–228.
- [55] P.C. Ford, Acc. Chem. Res. 14 (1981) 31–37.
- [56] P. Panagiotopoulou, D.I. Kondarides, J. Catal. 225 (2004) 327–336.